**BENIN JOURNAL OF PHYSICAL SCIENCES**
**BJOPS Vol. 1(1): page 1-18 (2024)**

# Metal Nanoclusters for Fluorescence Imaging

Hector H. OYEM

*School of Chemistry, Newcastle University, United Kingdom.*
*Department of Chemical Sciences, University of Delta, Agbor, Delta State, Nigeria.*

***Received:*** 27/04/2024 ***Accepted:*** 20/05/2024

**Abstract**

*The importance of metal nanoclusters (MNCs) and their remarkable opto-physical properties as inorganic fluorescent quantum dots for bio-imaging and applications in medical diagnosis were studied. Their significance as good replacements for oftentimes, less-effective organic analogues was demonstrated. Silver and copper nanoclusters were prepared by reducing their metal ions with sodium borohydride in aqueous solutions. Atomic force microscopy results showed that silver and copper nanoclusters with an average size of approximately 1.40 nm were synthesized from their salts. The presence of these MNCs was confirmed by confocal microscopy which also illustrated their luminescent and photostability properties. Fluorescence spectroscopy results showed that these samples possessed emissions at 435 and 617 nm for the AgNCs, and at 636 nm for the CuNCs excited at 315 and 255 nm respectively. Electrospray ionization mass spectrometer confirmed the presence of species with a metal core of $Ag_4$ and $Cu_7$ having a molecular mass of 529 and 559. Cyclic voltammetry data confirmed the presence of Ag (I) ions and Ag (0) in the sample solution. XPS similarly confirmed the elemental presence of these metals. Fluorescent quantum yield was ≈70 % which is remarkable for quantum dots. It was recommended that MNCs can present better effects as fluorescent probes for both bio-imaging and medical diagnosis.*

**Keywords:** *Fluorescence quantum dots, metal nanoclusters, quantum yield, AFM, bandgap.*

## 1. INTRODUCTION

Metal nanoclusters (MNCs) have gained a rave reputation for their unique optical properties. Their molecular-like sizes confer them with remarkable physical properties which are different from their bulk analogues. These metal nanoclusters



*Corresponding author, e-mail: hector.oyem@uidel.edu.ng; hectoroyem2013@gmail.com

(MNCs) are often less than 2 nm in size which is less than the Fermi wavelength of electrons (Cheng *et al*., 2014; Oyem, 2018; Yeh *et al*., 2011).

At these nanoscale sizes, these MNCs have large bandgaps as a result of their low density of state (Ahmed and Al-Baidhani, 2022; Teunis, Dolai and Sardar, 2014; Xie *et al.*, 2015; Xu and Suslick, 2010). The presence of these bandgaps enables the electronic transition from the valence to the conduction band according to Franck-Condon's principle upon interaction with requisite portions of the electromagnetic radiation. They therefore display absorption and emission properties which are characteristic of the bandgap (energy difference, $\Delta E$) between the valence and the conduction bands. The bandgap determines the wavelength of light absorbed and emitted during electronic transitions.

Medical sciences thrives on early detection and accurate diagnosis of infections and disease conditions. The essence of proper diagnosis is accompanied by effective treatment and management of patients, but all of these start at the point of detection which is key to effective healthcare delivery. Several disease detection methods presently available could do with some modification for effective healthcare administration in line with our contemporary times. One of these areas where such modification is required in the use of fluorescent dyes for imaging. Often times, a number of such dyes are deleterious and have been classified as either mutanogens or cancerous (Statements, 2017). An example is ethidium bromide which has been classified as a mutagen and toxic (Rationale, Health, Controls, Information, and Characterisation, 2020) but is widely used in DNA staining (Galindo-murillo and Cheatham, 2021). Whereas many methods of disease diagnosis tilt towards qualitative detection and less on the quantitative. Even then, the limits of detection is usually in the region of micrograms ($10^{-6}$).

The application of nanoscience and technology to medical science brings with it the properties of precision and sensitivity which are crucial to accurate detection of diseases and diagnosis even at femto- and atto-scales ($10^{-15}$ and $10^{-18}$) respectively (Liyanage *et al.*, 2018). The application of fluorescent nanoclusters (NCs) to medical science has the potential to replace the use of fluorescein and other quantum dots which in many instances are often poisonous and have low quantum yields with small Stokes shifts. Apart from possessing these advantages over the fluorescein and quantum dots, MNCs also possess the remarkable properties of being photostable (Malola *et al*., 2023; Matus and Häkkinen, 2023; Santillán *et al.*, 2020; Xiao *et al*., 2021) and can be applied to both *in vivo* and *in vitro* diagnosis. The metal ions can be attached to biomolecules to form complexes which can then be reduced to form nano-biomolecules with unique optical activities. The essence of this paper is to highlight the optical superiority and diagnostic advantages of MNCs of Ag and Cu over quantum dots and other fluoresceins.

## 2. MATERIALS AND METHODS

### 2.1 *Materials*

Silver nitrate ($AgNO_3$, 99.0 %) and sodium borohydride ($NaBH_4$, 99.0 %) from Sigma Aldrich, U.S.A. Copper nitrate ($Cu(NO_3)_2.3H_2O$, 98.0 %) Fluka Chemika, United Kingdom. Sodium bis-(2-ethyl hexyl) sulfosuccinate (AOT) ($C_2H_37Na0_7S$) from Sigma Aldrich, U.S.A, and 2,2,4-trimethylpentane (isooctane, 99.8 %) also from Sigma Aldrich, U.S.A. P-type silicon (111) wafer from Virginia Semiconductors, Virginia U.S.A. Nanopore water obtained from Millipore Diamond Barnstead series 1370, model D11931, operated at 100 – 240 V with a resistivity of 18.2 MΩ-cm manufactured by Barnstead International, Iowa, USA.

### 2.2 *Synthesis of aqueous solution of silver nanoclusters*

0.5 mM of AOT was dissolved in 5 mL isooctane in a beaker and the mixture was placed on a sonicator for 5 minutes. The resulting solution was shared into two halves; and 50 μL aqueous solution of 100 μM $AgNO_3$ and another 50 μL of 100 μM of $NaBH_4$ were added to either of the two portions of the AOT/isooctane. Then, the $NaBH_4$-AOT/isooctane was gradually added into the $AgNO_3$-AOT/isooctane portion and constantly stirred on a magnetic stirrer until the solution changes colour.

### *2.3 Synthesis of aqueous solution of copper nanoclusters*

0.5 mM of AOT was dissolved in 5 mL isooctane and sonicated for 5 minutes. The sonicated solution was then shared into two halves into which 50 μL aqueous solution of 100 μM of $Cu(NO_3)_2$ and another 50 μL of 100 μM of $NaBH_4$ were added to either of the two portions of the AOT/isooctane. Then, the $NaBH_4$-AOT/isooctane portion was gradually added into the $AgNO_3$-AOT/isooctane portion while constantly being stirred under a magnetic stirrer set at 350 rpm until the solution changes colour.

### 2.4 *Preparation of samples for fluorescence microscope imaging*

3 -5 mL deionized water was added to the as-synthesized nano-sized material in water-in-oil emulsion to break the emulsion system and effect a separate oil and water phase. The aqueous phase is separated from the oil phase using a separating funnel. The aqueous phase is passed through a chromatographic cartridge by Restek Corporation, USA containing reverse phase hydrophobic silica-based adsorbent capable of extracting non-polar substances from polar substrates, this was used to remove excess AOT surfactant under a vacuum pump. 1 – 2 μL portions of the eluted aqueous samples are drop-cast on a 1 $m^2$ silicon wafer previously cleaned with piranha solution and blow-dried using a stream of Argon

gas. The piranha-cleaned silicon chip containing the analyte sample was allowed to air-dry under vacuum condition in a fume cupboard overnight before obtaining fluorescence imaging using a ZEISS Axioskop2 plus model confocal microscope with equipped with a 100 W halogen lamp for transmitted light and a 50 W mercury arc lamp which reflected fluorescence light source; the instrument was operated at 240 V maximum.

### **2.5** ***Atomic Force Microscopy***

From the cartridge eluted sample above, another 1 – 2 μL is withdrawn onto another clean silicon wafer and similarly air-dried overnight before running on a Brukker Multimode 8 High-performance AFM instrument with High-Speed ScanAsyst at peak force tapping mode using a Vecco Incorporated Nanoprobe tips. Images were analyzed using Gwyddion 2.41 software.

### **2.6** ***Electrospray Mass Spectroscopy***

From the cartridge-separated aqueous phase sample, 1 μL aliquot portion was withdrawn into a micro-pipette and diluted 200 μL with deionized water to obtain a 1:200 dilution factor. This was then run through a Waters LCT Premier Electrospray ionization mass spectrometer for molecular mass analysis with a Masslynx 4.1 software and a time-of-flight analyzer.

### **2.7** ***X-ray Photoelectron Spectroscopy***

This sample was prepared following similar protocol as was the case with the fluorescence imaging. 1 – 2 μL of the aqueous-separated portion from the Restek cartridge was drop-casted onto a clean silicon wafer and air-dried overnight. The dried sample was put into a Kratos AXIS Nova X-ray photoelectron spectrometer manufactured by Kratos Analytical, Manchester, United Kingdom with a 1486.6 eV X-ray energy and a delay line detector (DLD). Data obtained were analysed using a CasaXPS software from casaxps.com.

### **2.8** ***Cyclic Voltammetry***

Cyclic voltammograms of silver nitrate aqueous solution were done using PSTrace 4.7 software with EnStat3 interphase by PalmSens BV, Electrochemical sensor interfaces, Netherlands.

## 3. RESULTS AND DISCUSSION

### 3.1 *Absorbance*

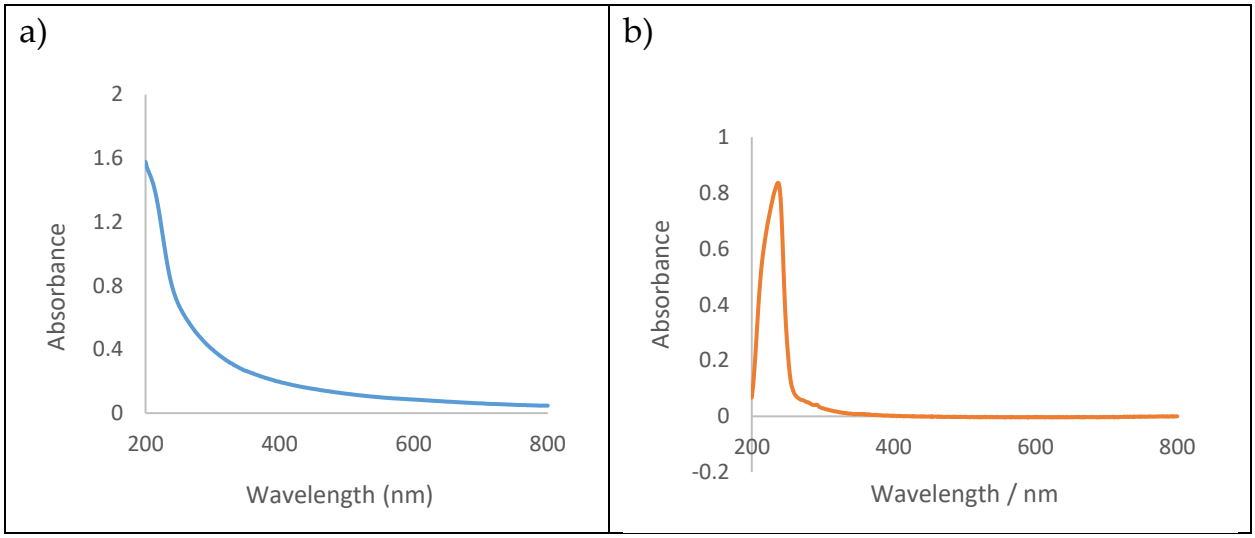


**Figure 1a & b:** Absorbance charts of Ag NCs and Cu NCs respectively formed from the emulsion system.

Figures 1a & b are absorbance charts of Ag NCs and Cu NCs respectively formed from the emulsion system. The absorbance (ABS) spectra shown above are distinct by the absence of surface plasmon resonance (SPR) bands for Ag and Cu. Usually, these resonance bands appear as a consequence of the formation of large NPs. Only large NPs whose sizes are already above 2 nm display SPR bands upon interaction with the uv-vis energy of the electromagnetic wave. Invariably, the absence of these SPR signals in the ABS spectra in Figures 1a & b is a testament to the absence of NPs of Ag and Cu. Instead, these spectra suggest the formation of NCs of Ag and Cu in emulsion systems. MNCs do not produce SPR due to their remarkable sizes which are indicative of molecular-size properties rather than bulk properties (Xu and Suslick, 2011). It's obvious from the ABS spectra of the samples in Figure 1, that Ag NCs and Cu NCs have been formed from their metal salts. The peak at 240 nm (asterisked) in Figure 1b is attributed to the d → d transitions of $Cu_n^{m+}$ species which are present in the aqueous solution (Kolwas and Derkachova, 2020; Li *et al.*, 2021; Lyu *et al.*, 2023).

### 3.2 *Fluorescence*

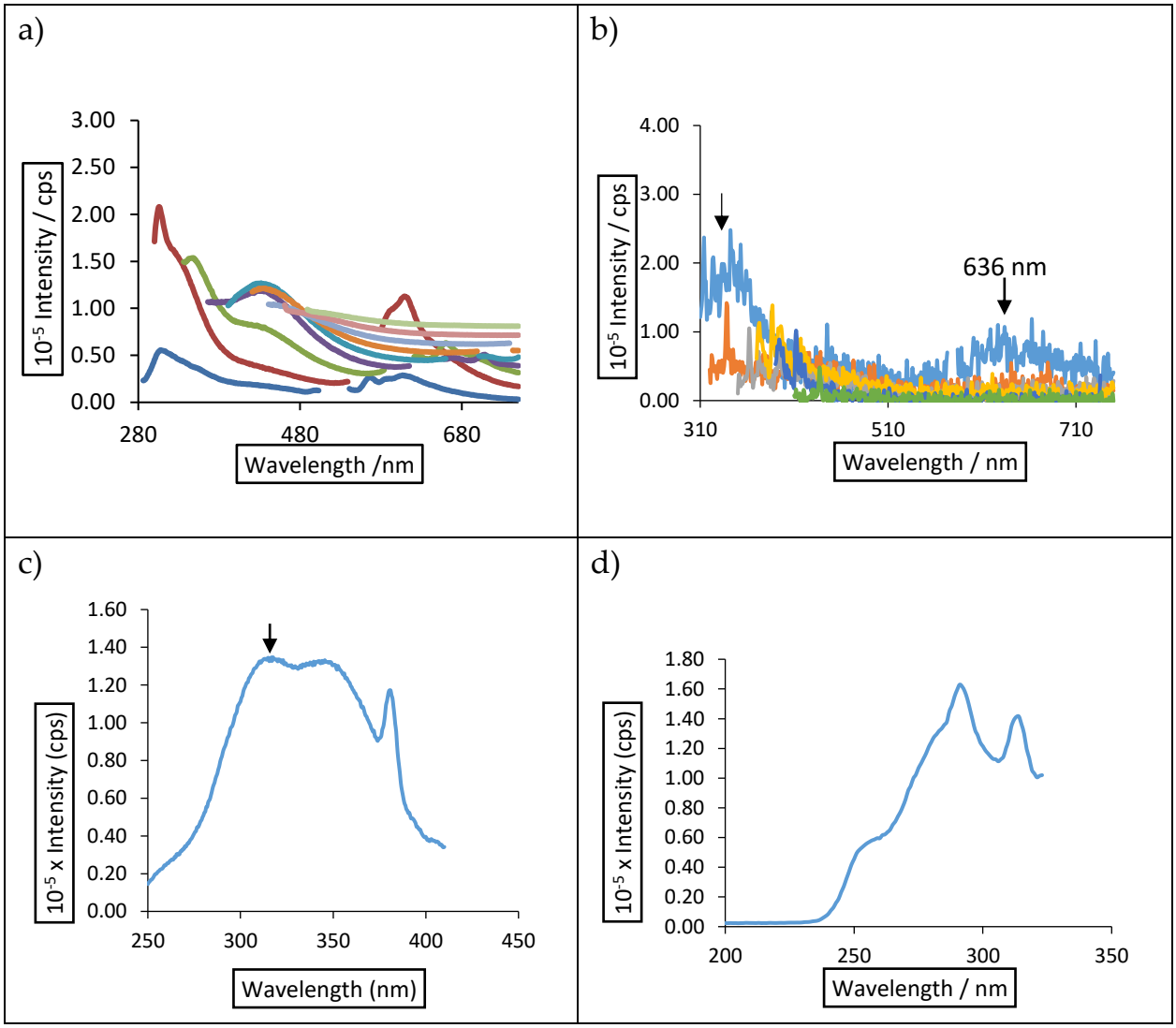


**Figure 2a, b, c & d:** Photoluminescence spectra of the as-synthesized a) Ag NCs; and b) of Cu NCs; while c) and d) are excitation spectra for Ag NCs and Cu NCs excited at 430 and 343 nm respectively; the red arrow at 380 nm indicates Raman peak for water.

From Figure 2a & b, we can readily discern the presence of multiple bands of fluorescence species. The spectrum in Figure 2a is that of Ag NCs showing emission bands at 315, 435, and 615 nm respectively. The band at 315 nm has been ascribed to signals from $Ag_4^{2+}$ (Antoku, 2007; Oyem, 2018; Oyem et al., 2022). These species are often formed immediately preceding the nucleation process of NCs/NP formation and growth (Antoku, 2007; Oyem, 2018). The band at 435 nm is attributed to emission signals due to $Ag_4$ – $Ag_6$ NCs (Oyem, 2018; Oyem et al., 2022). This band is not as intense as the first but broader with a higher full-width-at-half-maximum (FWHM). The third band at 615 nm is easily assigned to larger NCs of Ag from basic theory. Theoretically, the longer the wavelength of emission the larger the particle size. However, inadequate proportions of stabilizing ligands

can result in ineffective orbital overlap between resulting molecular orbitals. This can manifest in several vibrational states and the resultant deep trapped states with the consequence of long lifetimes in the excited states and loss of a significant amount of energy in non-radiative vibrational relaxation. In the end, only a small amount of residual excited energy is radiated as luminescence which expectedly occurs at longer wavelength with lower quantum yield.

Fluorescence quantum yield, $\phi = \frac{Photon\ emitted}{Photon\ received}$ (1)

$$\phi = \frac{2.85\ eV}{3.94\ eV}$$

$$\phi = 0.72$$

The quantum yield of 0.72 for the Ag NCs above is significant and shows that about 72 % of the photon absorbed/received is emitted after a short dark-phase lifetime. This underscores the credentials of these MNCs as a high-yielding fluorophore for fluorescence imaging and optical diagnosis. It is seldom to observe fluorescence quantum yields of more than 45 % with other fluorescein, especially of organic constituents.

The same explanation goes for the Cu NCs in Figure 2b where there are two bands of emission. This spectrum shows emission at 340 and 636 nm attributed to species of Cu NCs. The band at 340 nm is assigned to nucleated species of $Cu_n^{m+}$ species, while the band at 636 nm is suspected to be the Cu NCs band. The intensity and size of this 636 nm band is indicative that the Cu NCs population of this species is low concentration-wise.

Meanwhile, Figures 2c & d display the excitation spectra of the two Ag & Cu NCs. These spectra illustrate the excitation wavelengths of the excitons in the NCs. The peaks in these spectra typify the various exact excitation wavelengths of absorption for these MNCs. However, it is pertinent to note that the peak at 380 nm (indicated in red arrow) in Figure 2c is the Raman peak for water; this is not connected with the excitation wavelengths of the NCs. In general, the excitation wavelengths of the samples fall within the ultra-violet region of the electromagnetic spectrum which is synonymous with high energies, these translate that the "particles" are small (nanoscale) and also suggest that they possess large bandgaps (Cheng *et al.*, 2022; Xu and Suslick, 2010). Put together, the appearance of luminescence is a veritable conclusion of the fact that NCs rather than NPs have been formed; the latter would not exhibit any luminescence. This inference is supported by the results already explained in Figure 1 above where the usual SPR of large NPs was conspicuously absent.

### 3.3 *Fluorescence microscopy*

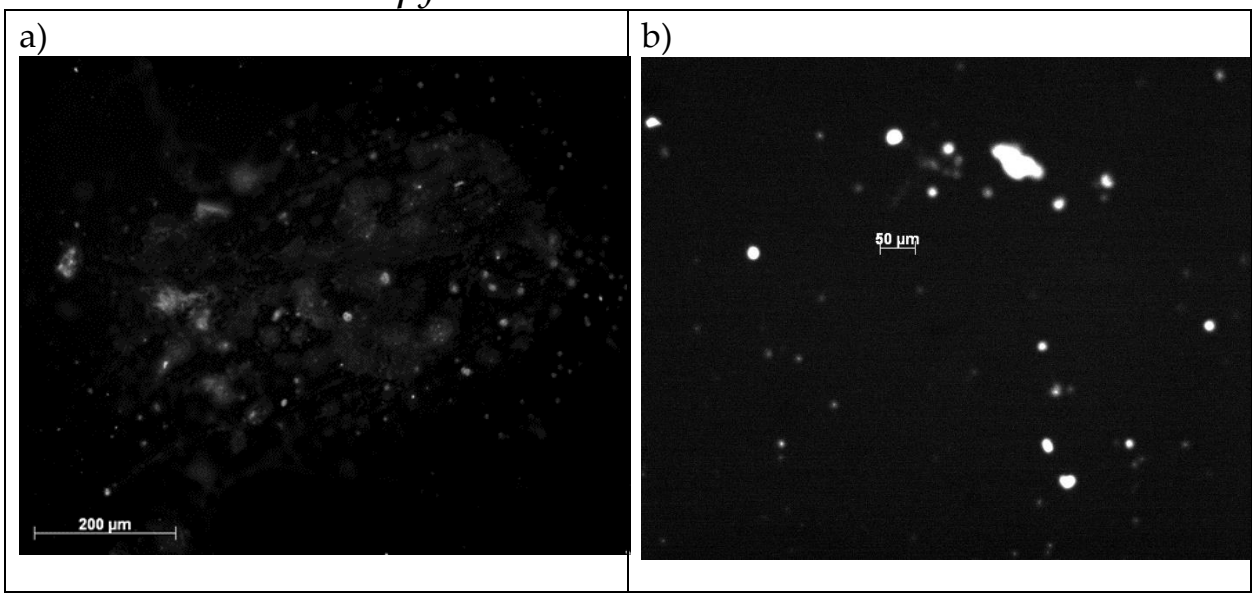


**Figure 3a & b:** Confocal microscopy images of the as-synthesized nano-materials, a) Ag NCs and b) Cu NCs.

The images in Figures 3a & b above are those of Ag and Cu NCs which are fluorescing. These are confocal microscope images which further confirms that the samples are luminescent. Again, the observation of luminescence from these samples is a testament to any claims that indeed NCs have been produced. Fluorescence microscopy is an important analytical tool used in nanoscience and nanotechnology. It combines both microscopy and luminescence techniques which enables researchers to observe the presence of particles as well as luminescence at the same time.

From the images in Figure 3, we can observe particles of Ag and Cu scattered about on clean silicon wafers of approximately 1 $m^2$. The image in Figure 3a is zoomed out at 200 µm and the small dots of Ag NCs can be seen fluorescing in the background. From the scale of this image, the sizes of these clusters can be resolved approximately to be in the nanoscale. The Cu NCs are zoomed in four times that of the Ag NCs image in Figure 3a, therefore the "particles" are bigger. Nonetheless, their larger sizes are linked to the agglomeration of several clusters in an attempt to reduce their larger surface-to-volume ratio. Similar agglomerated particles can be observed in the atomic force microscopy (AFM) images in Figure 4 below for the Ag NCs. The fact that these large particles are fluorescing is undoubtedly a confirmation of the fact that they are only a combination of individual clusters; otherwise, they wouldn't be fluorescing at their sizes.

Both Ag & Cu NCs had close to 60 s exposure time during the process of imaging the samples without photobleaching. These exposure time values indicate that the

samples are photostable and are advantageous compared with other quantum dots; these further highlight their credentials for optical imaging in life science.

**3.4** ***Atomic Force Microscopy***

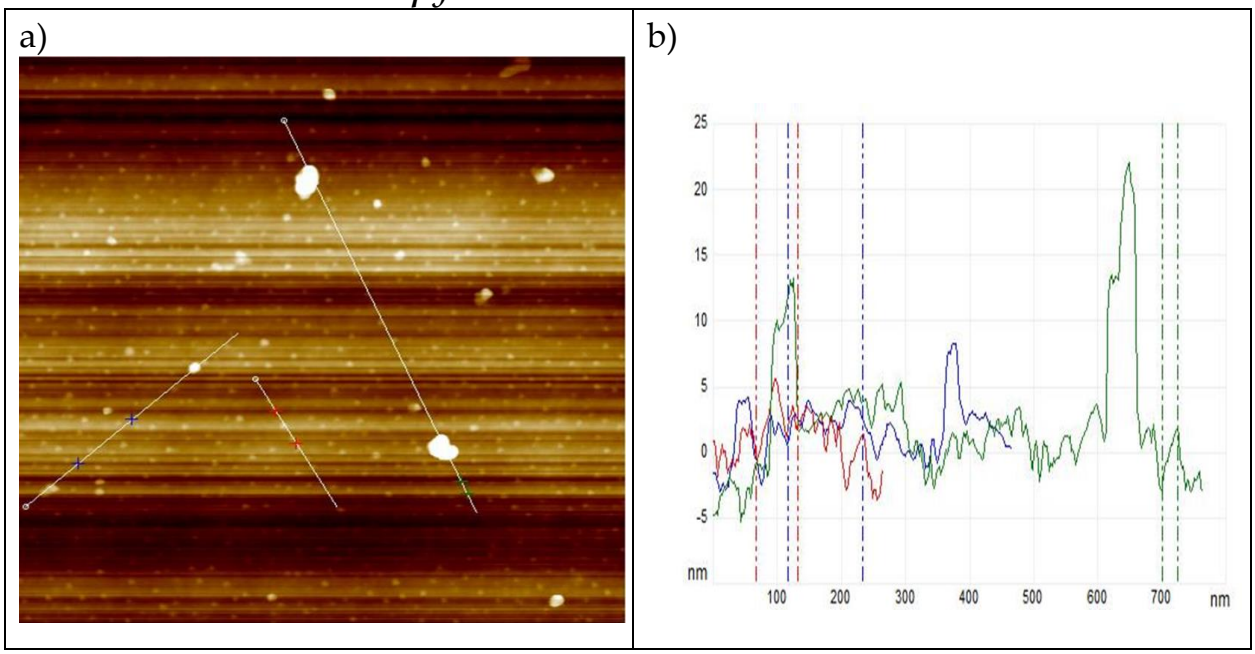


**Figure 4a & b:** AFM image of the Ag NCs sample obtained on a clean p-type silicon wafer showing straight lines which are used to obtain the height measurement; b) is the height chart (nm) of the same Ag NCs from the AFM instrument.

The AFM technique is an advancement over transmission electron microscopy (TEM), scanning electron microscopy (SEM) and confocal microscopy. Whereas the TEM and SEM techniques are limited in their provision of two-dimensional (2-D) data, the AFM has the unique property of providing three-dimensional (3-D) information on materials. One of the added information provided by the AFM machine amongst others is the height data of materials. This gives an accurate measurement of the size of materials, especially nanoparticles in the field of nanoscience and nanotechnology–material science. It obtains information by scanning through the material using the scan Assyst technology with a nanotip (Cantilever). As the Cantilever scans through the material, the force of repulsion between the material and the tip of the Cantilever is proportional to the height of the material being analyzed.

In Figure 4a above, we can see images of small clusters of Ag as well as several more conspicuous agglomerated Ag NCs earlier mentioned in the previous section above. These further give credence that NPs (indeed NCs) have been formed. Moreover, the more important information which necessitated the use of this device is presented in Figure 4b in the height data. Careful observation of this height chart shows that the majority of the particles are of an average size of < 2 nm. By dragging a line across several particles as shown in Figure 4a, a modal value of 1.40 nm was obtained for the cluster sizes. There are also apparently more

conspicuous larger particle sizes in the range of approximately 5 nm; that is, measuring from the 0 nm point (baseline). Three particles can be seen in the 10 to 15 nm size range which represents the large agglomerated NCs previously mentioned. Meanwhile, the AFM of the Cu NCs is not presented.

In Figure 5 below, the mass spectroscopy data of both the Ag NCs and Cu NCs are presented (Figure 5a & b respectively). This information was provided from the time-of-flight (TOF) electrospray ionization mass spectrometry analysis of the samples scanning at the negative mode of the instrument. The split patterns in Figures 5a & b are synonymous with $Ag_4$ and $Cu_7$ NCs. Their mass-to-charge (m/z) ratios of approximately 529 and 559 respectively also confirm their molecular masses (MMs). Whereas $Ag_4$ has an MM of 432, for $Cu_7$ it is 445; the balance is accounted for by the MM of the passivating ligand molecules around the cluster core acting as stabilizing agents. In this study, the following ligands were determined from the ESI-MS analyses to be the molecular formula of the ligands: $B_3O_4$ (MM=97), and $B_3O_5$ (MM=113) for the Ag and Cu NCs respectively. The presence of these functional groups was confirmed by an infrared spectrophotometer (Figure 6a, b & c).

### 3.5 *Electrospray mass spectroscopy*

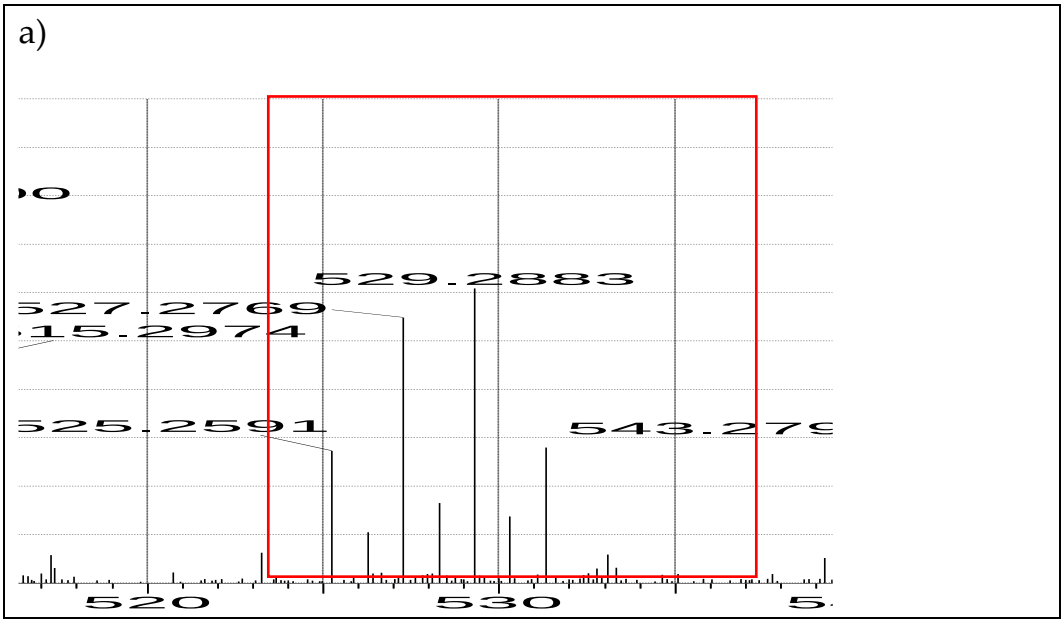

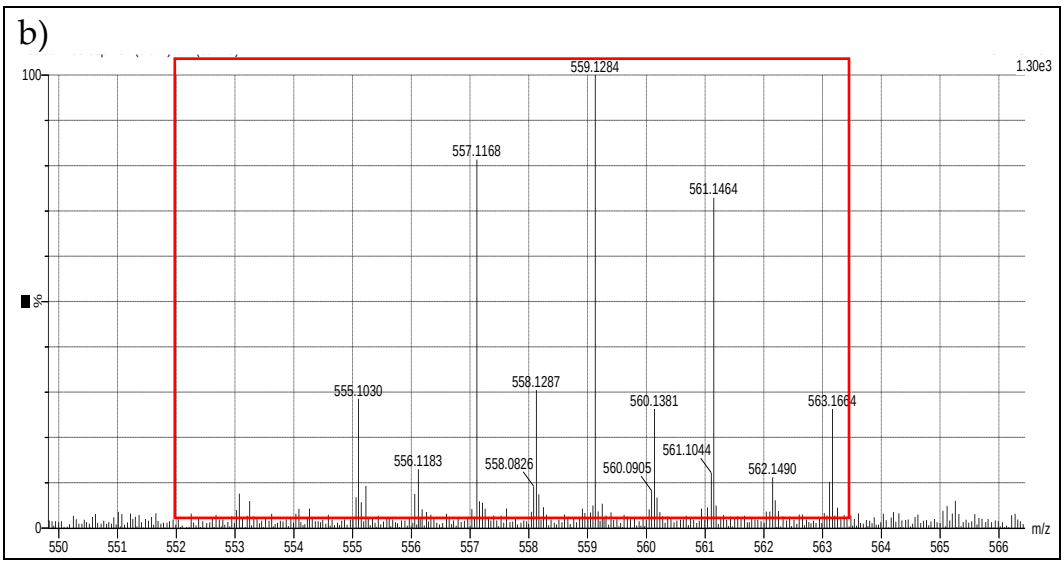


**Figures 5a & b:** ESI-MS data for a) the Ag NCs with a molecular mass of 529, and b) Cu NCs with a molecular mass of 559. The horizontal axes show the m/z ratio, while the vertical axes represent the isotopic abundance.

### 3.6 *Fourier Transform Infrared Spectroscopy*

For the purpose of characterizing and confirming the ligand shell around the metal core of the NCs, Fourier Transform Infrared spectroscopy (FT-IR) data of the samples were obtained and presented in Figure 6a, b & c.

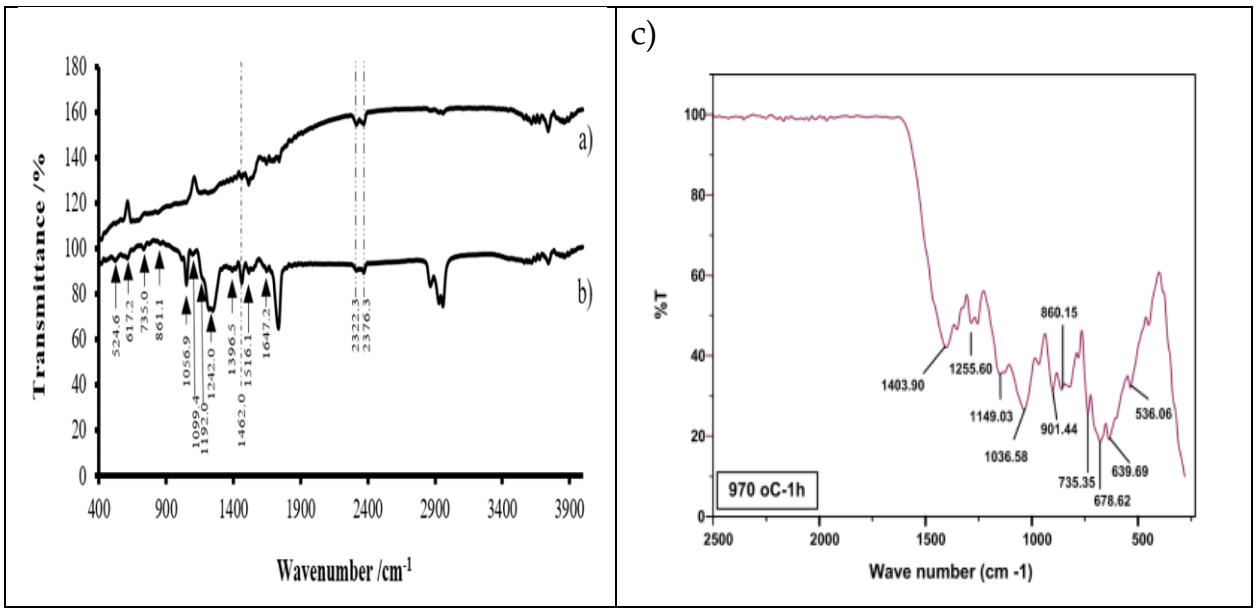


**Figure 6a, b & c:** FT-IR spectra of the ligand shell of the NCs showing signals of the various functional groups present in the ligand shell; a) 100 µM b) 1 mM (optimized sample). IR spectra of the NCs are identical; c) IR spectrum of calcium borate nanoparticles by Erfani *et al.,* (2012).

Since the signals in the original samples is weak, it was necessary to optimized these signals by increasing the sample concentration and therefore obtain better resolution; this was shown in the spectrum in Figure 6b above. Several weak bands can be discerned in the fingerprint region of the spectrum in Figure 6b representing various types of bending and stretching vibrations. However, the bands relating to the borate group ($B_3O_5$) and associated with the various **B-O** bonds in the molecule can be seen at 524, 617, 735, 861, 1006, 1192, 1242, and 1395 $cm^{-1}$ representing various bending and stretching vibrational bands of the $B_2O_3$ ligand. This result is consistent with similar values reported by (Erfani *et al*., 2012; Gautam *et al*., 2012) on the IR spectrum of calcium borate nanoparticles in Figure 6b above. This confirms the presence of borates as the passivating ligands of the Ag and Cu NCs in this study. Meanwhile, the bands at 1800 and 3150 $cm^{-1}$ are typical bands corresponding to the $C{=}O_{str}$ and $C{-}H_{str}$ vibrations which are associated with the surfactant (AOT) molecule.

### 3.7 *Cyclic Voltammetry*

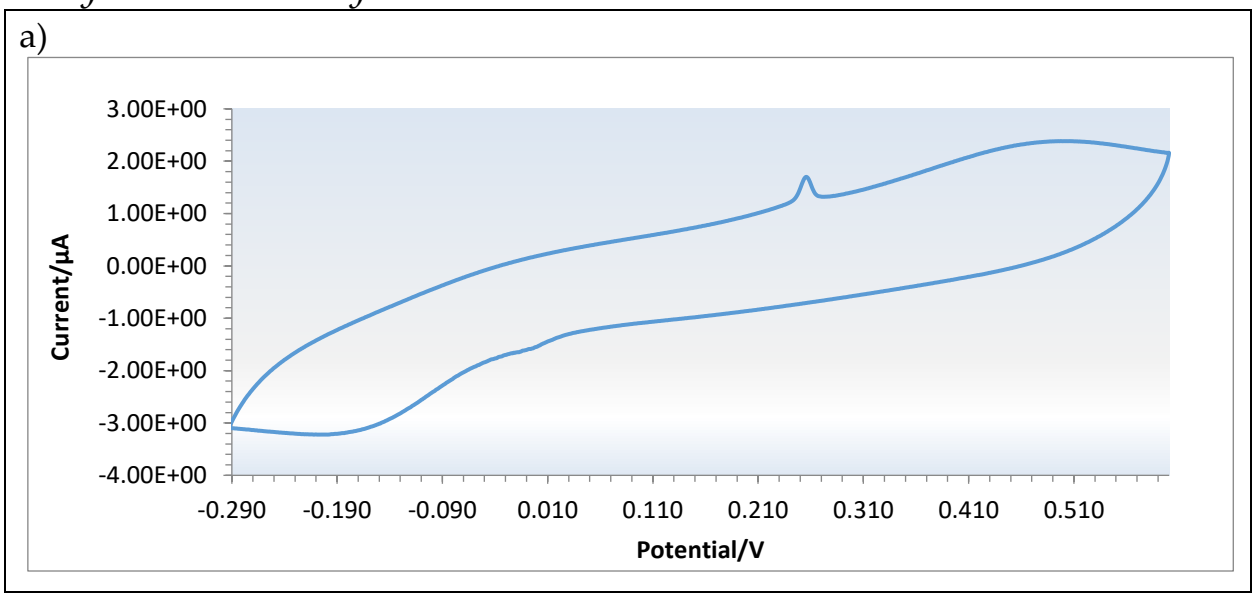

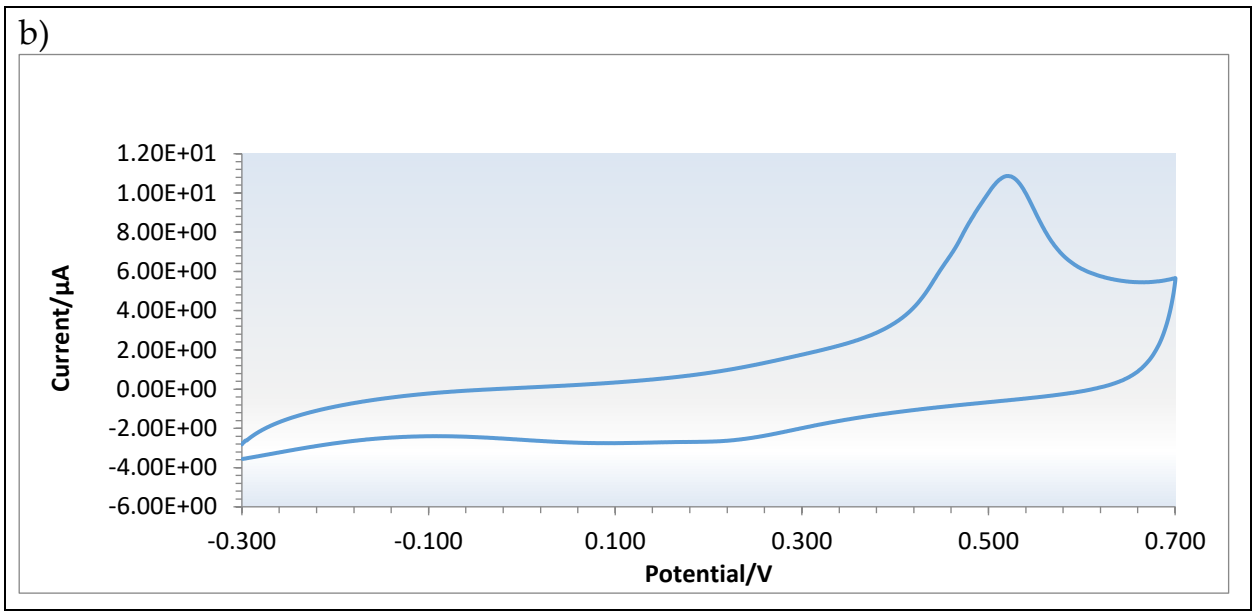


**Figure 7a & b:** Cyclic Voltammograms of a) 100 µM $AgNO_3$ and b) 1 mM $AgNO_3$ aqueous solutions at a scan rate of 0.5 s.

Samples of the $AgNO_3$ were photo-reduced in a Rayonet photochemical reactor manufactured by the South England Ultraviolet company, USA; the instrument has a mercury source light with an emission wavelength set at 254 nm. Figure 7a is the cyclic voltammograms of the 100 µM of the $AgNO_3$ showing a weak reduction peak at 0.270 V. This shows that the sample contained Ag (I) ions in the aqueous solution which were reduced to metallic Ag. However, since the peak obtained for the 100 µM sample in Figure 7a was weak which is expected since the electrochemical technique is one of the most sensitive and reliable analytical tools, however, for emphasis, the analysis was repeated using a 1 mM sample as indicated in Figure 7b for emphasis to highlight the fact that samples contained Ag (I) ions which were reduced to Ag (0) even though the 100 µM $AgNO_3$ voltammogram in Figure 7a still shows small traces of Ag (I) ions in solution. More so, since in cyclic voltammetry, the area under the peak is directly proportional to the concentration of the analyte. Cyclic voltammetry scans between a given range of reduction potential and then switches in the reverse direction this time scanning through the same range of electrode potentialsto obtain the oxidation potentials of the electrochemical species in the solution. .

### 3.8 *X-ray photoelectron spectroscopy*

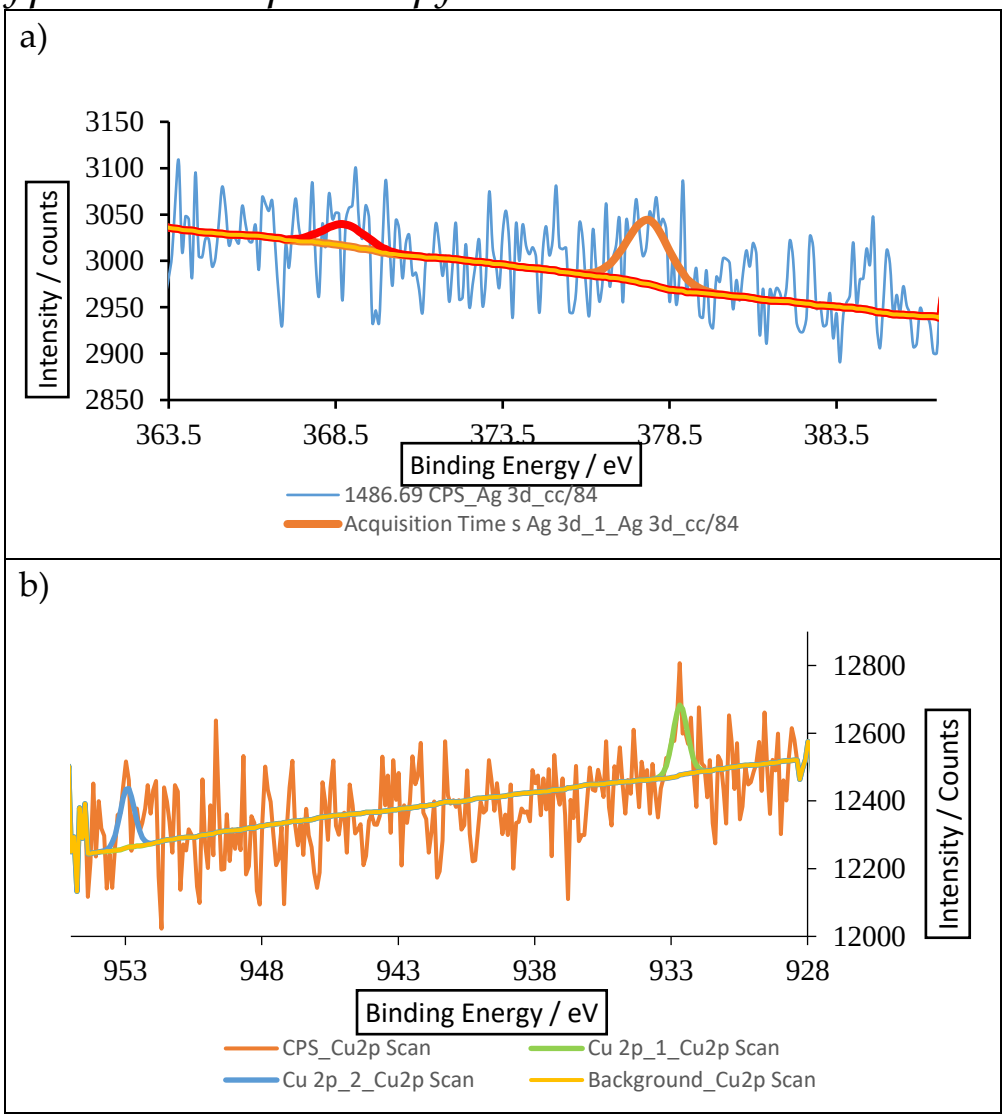


**Figure 8a & b:** X-ray photoelectron spectroscopy data of a) the Ag NCs and, b) Cu NCs samples.

In order to confirm the presence of the Ag and Cu species in the samples, it was necessary to carry out an elemental analysis using the X-ray photoelectron spectrometry (XPS) technique. The XPS technique works by hitting an analyte sample with incident X-rays, this ejects electrons from their orbitals and the kinetic energy (in eV) of the ejected electrons is measured as this provides information about the particular shell from which these electrons are domiciled in a given atom of an element. Diluted portions of the sample which were used for the microscopic studies were presented for XPS analyses. Data from this instrument obtained for the samples are presented in Figure 8a & b. Although, the resolution of the chart is poor owing to the extremely dilute nature of the sample which accounts for the high noise background as the instrument is concentration sensitive; signals corresponding to Ag $3d_{5/2}$ and Ag $3d_{3/2}$ can be resolved at approximately 368.5 and 378.5 eV from Figure 8a. These are in tandem with XPS values for Ag reported in

the literature (Firet *et al*., 2019; Mikhlin *et al*., 2011; Mikhlin *et al*., 2018; Simon *et al*., 2022). Similarly, values of 933 and 953 eV can be observed corresponding to Cu $2p_{3/2}$ and Cu $2p_{1/2}$ respectively and matching with data reported for Cu by researchers in the National Institute of Standards and Technology (NIST) database (Naumkin et al., 2023).

These results invariably confirm that the particles on the silicon wafer which we have seen from the various microscopic images already displayed in this study are indeed Ag and Cu NCs. XPS data were also obtained which confirmed the presence of signals of boron and oxygen, however, these are not presented here.

## 4. CONCLUSİON

The credentials of MNCs as veritable candidates for fluorescence imaging in medical diagnostics were highlighted in this study. Results showed their strengths over other quantum dots particularly of organic sources, especially in terms of their photostability, cost and relative toxicity. The fluorescence quantum yield of these MNCs is among the highest and typifies low Stokes shift and short lifetimes. MNCs in addition to possessing the advantage of precision offer the combined attributes of selectivity and sensitivity in the detection and quantification of analytes in analytical studies. *In vitro* and *in vivo* studies would certainly benefit from the unique optical properties of these MNCs in the field of sensors and medicine.

## CONFLICTS OF INTEREST

No conflict of interest was declared by the authors.

## REFERENCES

[1] Ahmed, A. M., and Al-Baidhani, J. H. (2022). Spatial, Temporal Variation of Physio-Chemical Properties in Tigris River within Baghdad City, Iraq. *Nigerian Society of Physical Sciences*, *4*(2), 287–600. doi:10.5281/zenodo.7506681

[2] Antoku, Y. (2007). Fluorecent Polycytosine-Enxapsulated Silver Nanoclusters (Georgia Institute of Technology). Georgia Institute of Technology. Retrieved from http://hdl.handle.net/1853/14568

[3] Cheng, D., Liu, R., and Hu, K. (2022). Gold nanoclusters: Photophysical properties and photocatalytic applications. *Frontiers in Chemistry*, *10*(July), 1–17. doi: 10.3389/fchem.2022.958626

[4] Erfani, M., Saion, E., Soltani, N., Hashim, M., Saffiey, W., Abdullah, B. W.,

and Navasery, M. (2012). *Facile Synthesis of Calcium Borate Nanoparticles and the Annealing Effect on Their Structure and Size*. (April 2014). doi: 10.3390/ijms131114434

[5] Firet, N. J., Blommaert, M., Burdyny, T., Venugopal, A., Bohra, D., Longo, A., and Smith, W. A. (2019). Operando EXAFS Study Reveals Presence of Oxygen in Oxide-derived Silver Catalysts for Electrochemical $CO_2$ Reduction. *Journal of Materials Chemistry A*, 7, 2597–2607.

doi: https://doi.org/10.1039/C8TA10412C

[6] Galindo-murillo, R., and Cheatham, T. E. (2021). Ethidium bromide interactions with DNA : an exploration of a classic DNA – ligand complex with unbiased molecular dynamics simulations. *49*(7), 3735–3747. doi: 10.1093/nar/gkab143

[7] Gautam, C., Yadav, A. K., and Singh, A. K. (2012). A Review on Infrared Spectroscopy of Borate Glasses with Effects of Different Additives. *2012*. doi:10.5402/2012/428497

[8] Kolwas, K., and Derkachova, A. (2020). Impact of the Interband Transitions in Gold and Silver on the Dynamics of Propagating and Localized Surface Plasmons. *Nanomaterials*, *10*(7), 1–27. doi: 10.3390/nano10071411

[9] Li, J., Zhu, J. J., and Xu, K. (2014). Fluorescent metal nanoclusters: From synthesis to applications. *TrAC - Trends in Analytical Chemistry*, *58*, 90–98. doi: 10.1016/j.trac.2014.02.011

[10] Li, Y., Liao, Y., Zhang, J., Huang, E., Ji, L., Zhang, Z., … Qin, G. (2021). High-Entropy-Alloy Nanoparticles with Enhanced Interband Transitions for Efficient Photothermal Conversion. *Angewandte Chemie - International Edition*, *60*(52), 27113–27118. doi: https://doi.org/10.1002/anie.202112520

[11] Liyanage, T., Rael, A., Shaffer, S., Zaidi, S., Goodpaster, J. V., and Sardar, R. (2018). Fabrication of a Self-assembled and Flexible SERS Nanosensor for Explosive Detection at parts-per-quadrillion Levels from Fingerprints. *Analyst*, *143*(9), 2012–2022. doi: 10.1039/c8an00008e

[12] Lyu, P., Espinoza, R., and Nguyen, S. C. (2023). Photocatalysis of Metallic Nanoparticles: Interband vs Intraband Induced Mechanisms. *The Journal of Physical Chemistry C*, *127*(32), 15685–15698.

doi: https://doi.org/10.1021/acs.jpcc.3c04436

[13] Malola, S., Matus, M. F., and Häkkinen, H. (2023). Theoretical Analysis of the Electronic Structure and Optical Properties of DNA-Stabilized Silver Cluster $Ag_{16}C_{l2}$ in Aqueous Solvent. *The Journal of Physical Chemistry C*, *127*(33), 16553–16559. doi: https://doi.org/10.1021/acs.jpcc.3c04103

[14] Matus, M. F., and Häkkinen, H. (2023). Understanding Ligand-protected Noble Metal Nanoclusters at Work. *Nature Reviews Materials*, *8*(2023). doi:

https://doi.org/10.1038/s41578-023-00537-1

[15] Mikhlin, Y., Karacharov, A., Likhatski, M., Podlipskaya, T., Zubavichus, Y., Veligzhanin, A., and Zaikovski, V. (2011). Submicrometer intermediates in the citrate synthesis of gold nanoparticles: New insights into the nucleation and crystal growth mechanisms. *Journal of Colloid and Interface Science*, *362*(2), 330–336. doi: 10.1016/j.jcis.2011.06.077

[16] Mikhlin, Y. L., Pal'yanova, G. A., Tomashevich, Y. V., Vishnyakova, E. A., Vorobyev, S. A., and Kokh, K. A. (2018). XPS and Ag L3-edge XANES Characterization of Silver and Silver–Gold Sulfoselenides. *Journal of Physics and Chemistry of Solids*, *116*(2018), 292–298.

doi: https://doi.org/10.1016/j.jpcs.2018.01.047

[17] Naumkin, A. V., Kraut-Vass, A., Gaarenstroom, S. W., and Powell, C. J. (2023). *NIST X-ray Photoelectron Spectroscopy Database*.

doi: https://dx.doi.org/10.18434/T4T88K

[18] Oyem, Hector H., Houlton, A., and Horrocks, B. R. (2022). Silver Nanoclusters Prepared in Water-in-oil emulsions. *Nano Express*, *3*(4). doi: 10.1088/2632-959X/acb83a

[19] Oyem, Hector Henry. (2018). *Fluorescence Silver Nanoclusters*. University of Newcastle, upon Tyne, United Kingdom.

[20] Rationale, G., Health, E. W., Controls, S., Information, H. H., and Characterisation, R. (2020). *Fluorescein and its sodium salt : Human health tier II assessment Import , Manufacture and Use*. (July 2016), 1–13.

[21] Santillán, J. M. J., Arboleda, D. M., Muraca, D., Schinca, D. C., and Scaffardi, L. B. (2020). Highly fluorescent few atoms silver nanoclusters with strong photocatalytic activity synthesized by ultrashort light pulses. *Nature Scientific Report*, *10*(8217). doi: https://doi.org/10.1038/s41598-020-64773-z

[22] Simon, P., Baldovino-Medrano, V.G., and Wojcieszak, R. (2022). X-Ray Photoelectron Spectroscopy (XPS): Principles and Application for the Analysis of Photoactive Materials. In A. O. T. Bahnemann, D., Patrocinio (Ed.), *Springer Handbook of Inorganic Photochemistry. Springer Handbooks.* Springer, Cham. doi: https://doi.org/10.1007/978-3-030-63713-2_10

[23] Statements, H. (2017). *Ethidium Bromide ( EtBr )*.

[24] Teunis, M. B., Dolai, S., and Sardar, R. (2014). Effects of Surface-passivating Ligands and Ultrasmall CdSe Nanocrystal Size on the Delocalization of Exciton Confinement. *Langmuir*, *30*(26), 7851–7858. doi: 10.1021/la501533t

[25] Xiao, D., Qi, H., Teng, Y., Pierre, D., Kutoka, P. T., and Liu, D. (2021). Advances and Challenges of Fluorescent Nanomaterials for Synthesis and Biomedical Applications. *Nanoscale Research Letters*, *16*(167). doi: https://doi.org/10.1186/s11671-021-03613-z

[26] Xie, Y., Teunis B. M., Pandit, B., Sardar, R, and Liu, J. (2015). Molecule-like CdSe Nanoclusters Passivated with Strongly Interacting Ligands: Energy Level Alignment and photoinduced Ultrafast Charge Transfer Processes. *Journal of Physical Chemistry C*, *119*, 2813–2821. doi: 10.1021/jp510276c

[27] Xu, H., and Suslick, K. S. (2010). Water-soluble Fluorescent Silver Nanoclusters. *Advanced Materials*, *22*(10), 1078–1082.

doi: 10.1002/adma.200904199

[28] Yeh, Hsin-Chih, Sharma, Jaswinder, Han, J. Jason, Martinez, S. Jennifer, and Werner, H. J. (2011). A Beacon of Light: A New Molecular Probe for homogeneneous Detection of Nucleic acid targets. *IEEE Nanotechnology Magazine*, 28–33. doi: 10.1109/MNANO.2011.940951